analytical chemistry

pubs.acs.org/ac Article

Atom Probe Mass Spectrometry of Uranium Isotopic Reference Materials

Frederick Meisenkothen,* Mark McLean, Irina Kalish, Daniel V. Samarov, and Eric B. Steel

Cite This: *Anal. Chem.* 2020, 92, 11388–11395 Read Online

ACCESS | Metrics & More | Article Recommendations | Supporting Information

ABSTRACT: Atom probe tomography (APT)-based isotopic analyses are becoming increasingly attractive for analysis applications requiring small volumes of material and sub-micrometer length scales, such as isotope geochemistry, nuclear safety, and materials science. However, there is an open question within the atom probe community as to the reliability of atom probe isotopic and elemental analyses. Using our proposed analysis guidelines, in conjunction with an empirical calibration curve and a machine learning-based adaptive peak fitting algorithm, we demonstrate accurate and repeatable uranium isotopic analyses, via atom probe mass spectrometry, on U_3O_8 isotopic reference materials. By using isotopic reference materials, each measured isotopic abundance value could be directly compared to a known certified reference value to permit a quantitative statement of accuracy. The isotopic abundance measurements for ^{235}U and ^{238}U in each individual APT sample were consistently within ±1.5% relative to the known reference values. The accuracy and repeatability are approaching values consistent with measurements limited primarily by Poisson counting statistics, i.e., the number of uranium atoms recorded.

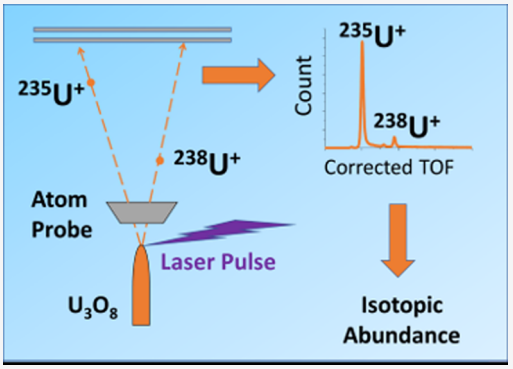

The atom probe tomography (APT) instrument has been described as a time-of-flight mass spectrometer coupled with a point projection microscope.[1] In atom probe analyses, a needle-like specimen is subjected to a high applied electric field to lower the energy barrier to the field evaporation of ions. A laser pulse or a voltage pulse is used to promote a "controlled" ion evaporation event and to signal the start of the time-of-flight (TOF) measurement. Ideally, only one ion will be emitted and detected in association with a given pulse event (a single-hit detection event); however, multiple ions can also be emitted and detected on a single pulse event (a multihit detection event). The ion impact positions on a two-dimensional (2-D) position-sensitive ion detector and the ion arrival sequence can, together, be used to produce a three-dimensional (3-D) reconstruction of the specimen atom by atom. The ion identities are determined from the TOF information. While atom probe microscopy has been around for over 50 years,[2] only within the last 15 years has the technique enjoyed widespread use in a variety of applications (100+ instruments now installed in 18+ countries). The convergence of several recent enabling technologies was required to make this possible: (1) the local electrode increased the field of view by an order of magnitude and allowed ion detection rates up to 4 orders of magnitude higher than in previous instruments (ca. 2003), (2) high-speed central processing units and graphical processing units capable of processing data sets containing hundreds of millions of ions were developed, (3) commercial vibration-isolated mechanical refrigeration systems became available (ca. 2000), (4) suitable, commercially available, stable, small-spot lasers were created (ca. 2006), and (5) it became possible to use focused ion beam scanning electron microscope (FIB-SEM) instruments for site-specific sample extraction and for the preparation of atom probe specimen tips (ca. 2005).[3] With these advances, the time required for atom probe data acquisition and analysis became practical, and a much broader range of specimen materials could be analyzed, e.g., electrically and thermally non-conductive oxide materials and particles.

APT has the highest spatial resolution of any mass spectrometry technique and can provide near-atomic-resolution chemically and isotopically resolved images. APT specimens must have a sharp needle-like geometry, with a tip diameter typically less than ~200 nm;[1] however, numerical modeling has shown that, for specimen tip diameters <500 nm, it is theoretically possible to generate an electric field high enough for evaporation to proceed in a local electrode atom probe (LEAP) instrument.[4] Larger specimen materials can be used, but they must be reduced in size via FIB-SEM, or some

Received: May 27, 2020
Accepted: July 22, 2020
Published: July 22, 2020

other means, prior to analysis in the atom probe. In APT, all elements are ionized with equal, and near 100%, efficiency, and the ion-species-independent detection efficiency can approach 80%. The high detection efficiency of APT provides a significant advantage over other mass spectrometry techniques when analyzing small volumes of material, like the powdered reference material used in this study. For comparison, thermal ionization mass spectrometry (TIMS) or secondary ion mass spectrometry (SIMS) is commonly used to measure the isotopic abundances of ^{234}U, ^{235}U, ^{236}U, and ^{238}U. However, due to the low combined ionization and transmission efficiency for uranium, these two mass spectrometry techniques require an analysis volume roughly an order of magnitude larger than that required by APT to achieve a comparable level of measurement uncertainty. Moreover, APT ideally does not require matrix correction algorithms or relative sensitivity factors to convert measured ion counts to fractional abundances. NanoSIMS offers a high lateral spatial resolution but suffers from low count rates (due to the use of probe currents an order of magnitude smaller than those typically used for SIMS), low ionization efficiency, and sensitivity variations between different phases.[5,6] Likewise, laser ablation inductively coupled plasma mass spectrometry has been explored for measuring the isotopic composition of single uranium particles, but the useful ion yield when analyzing uranium is similarly low, with values between 0.01% and 2.8%.[7] Hence, APT is becoming increasingly attractive for analysis applications requiring small volumes of material and submicrometer length scales, such as geological materials and geochronology;[8−10] nuclear fuels and nuclear forensics,[6,11−16] semiconductor materials,[17−21] and meteoritic materials.[22−26] Unfortunately, it has been demonstrated that quantitative analyses in the atom probe can be unreliable. Often, the chemical composition or isotopic abundance must be known *a priori*, or additional information (e.g., correlative data from an independent analysis technique) is needed to lend confidence to the results obtained via the atom probe.[13,27−36] Further, no community-wide accepted practices for assigning regions of interest in the mass spectrum (or TOF spectrum) to specific ion species (e.g., UO_2^{2+}, UO_2^{+}, or UO_3^{+}) have been defined. The accuracy for interelement and isotopic analyses can frequently exceed ±10% relative error and may not be reproducible between replicate measurements on the same material.[13,36] [Percent relative error is here defined as 100% × (measured value − reference value)/reference value.]

In a prior paper, we demonstrated how the results of an atom probe quantitative analysis can vary widely with the method used to assign ion species to regions of interest in the mass spectrum (or TOF spectrum).[37] Also, multihit detection events were found to have a significant and adverse effect on isotopic analysis results. However, using the following guidelines, we were able to demonstrate accurate isotopic analyses, even for data sets containing an exceedingly high fraction of multihit detection events: (a) analyze the corrected TOF spectrum (timing-signal-only based), using a bin width of 0.01 ns or less; (b) filter the data set to remove as many multihit detection events as possible; (c) treat each ion species as a separate measurement for isotopic abundance; (d) assume all isotopic variants of a given ion species have the same peak form; (e) use an optimization algorithm to determine an estimate of the common peak form shared by the isotopic variants of a given ion species; (f) pool the isotopic abundance measurements obtained from each ion species to report the isotopic abundance for the specimen (e.g., averaging).[37]

In the present study, we employed our proposed analysis guidelines, in conjunction with an empirically determined calibration curve, to obtain accurate and repeatable uranium isotopic analyses, via atom probe mass spectrometry, in U_3O_8 certified isotopic reference materials. The reference materials used are part of a suite of 18 uranium isotopic standards that had been certified as standard reference materials (SRMs) by the National Bureau of Standards (now the National Institute of Standards and Technology, NIST). The ^{235}U enrichment levels in these reference materials included natural uranium, low enriched uranium (LEU), and highly enriched uranium (HEU). The original purpose of these SRMs was to serve as quality control standards within the Atomic Energy Commission complex, and the initial isotopic composition measurements were completed in 1959.[38] In the 1980s, custody of the uranium isotopic SRMs was transferred to The U.S. Department of Energy (DOE) New Brunswick Laboratory and the SRMs were rebranded as certified reference materials (CRMs). These uranium isotopic standards comprise one of the most extensive sets of isotopic standards with known absolute isotopic compositions for any element. The SRMs have, therefore, also found application in evaluating and calibrating mass spectrometers, because they offer a uniform set of standards with a wide range of isotopic abundances—it is for this reason that we chose to use these isotopic standards to evaluate our measurement methods for accuracy and repeatability. By using isotopic reference materials, each measured isotopic abundance value could be directly compared to a known certified reference value to permit a quantitative statement of accuracy. Though our measurement focus was on the ^{235}U, we also report measurement results for ^{238}U and ^{234}U. The ^{236}U isotope was also detected, but the quantification of this isotope is left for future work. Despite the high number of multihit detection events in each data set, no deadtime correction algorithms were necessary to obtain accurate results.

MATERIALS AND METHODS

Specimen Preparations. Four uranium isotopic reference materials were used in this study: CRM 129-A (U-Nat), SRM U-030A (LEU), SRM U-350 (HEU), and SRM U-900 (HEU). The ^{235}U abundance levels range from U-Nat (0.72% ^{235}U) to HEU (90% ^{235}U). Each reference material consists of U_3O_8 in powdered solid form. For analysis, a small amount of each reference material was deposited on its own dedicated silicon or carbon planchet. The certified isotopic abundance values for each of these reference materials can be found in Table 1.

Two dual-beam FIB-SEM instruments with *in situ* micromanipulator systems were employed to prepare all particle specimens for the atom probe analyses. Conventional lift-out

Table 1. Certified Isotopic Abundance Values for the Reference Materials

	uranium isotope (atom %)			
	234	235	236	238
CRM 129-A	0.005296	0.72087	0.0000097	99.27382
SRM U-030A	0.02778	3.0404	0.000599	96.9312
SRM U-350	0.2498	35.19	0.1673	64.393
SRM U-900	0.7777	90.196	0.3327	8.693

https://dx.doi.org/10.1021/acs.analchem.0c02273
Anal. Chem. 2020, 92, 11388−11395

techniques and ion-milling procedures were used throughout the work.[39−41] The FEI Helios NanoLab 660 FIB-SEM instrument was equipped with an FEI EasyLift micromanipulator, and the FEI Nova NanoLab 600 instrument was equipped with an OmniProbe 200 micromanipulator. The picked particles were placed on commercially available CAMECA silicon flat-top-post specimen support coupons. The particles picked from each reference material planchet were within the size range of 825 nm ±375 nm. The particles were then ion-milled to a needle-like shape, having a tip diameter of <200 nm for atom probe analysis. Isotopic analysis results for 28 different particles are presented in this paper.

Data Acquisition. A CAMECA, Inc. LEAP 4000X-Si instrument, with a straight flight path of 90 mm, was used to collect all atom probe data associated with this study. The instrument was operated in the laser-pulsed mode (UV, λ = 355 nm) with the polarization direction fixed parallel to the long axis of the specimen.[42] The estimated ion detection efficiency of the instrument is ∼50%.[43] A trial-and-error process was used to determine a set of acquisition conditions for which the U_3O_8 specimens would typically survive long enough in the atom probe to yield usable data sets.[15] Except where noted, the specimens were run under the following general conditions: T = 57 K; detection rate (DR) = 1%; laser pulse frequency = 250 kHz; laser pulse energy = 1 or 2 pJ. Replicate measurements were made for each reference material, with each replicate being conducted on a different individual particle specimen. The acquisition conditions for each specimen are provided in Table S1 (in the Supporting Information). The fraction of multihit detection events reported by the instrument for these samples was typically around 0.34 (34%). The total number of uranium ion counts recorded in any one data set was between ∼8.3×10^5 and ∼30×10^6 counts, and every ion species used for quantification possessed >1.2×10^5 ion counts (Table S2).

Data Analysis. A 3-D chemically and isotopically resolved spatial reconstruction of the ions collected for each data set was created within the CAMECA Integrated Visualization and Analysis Software (IVAS) (v3.6.14, v3.8.2). Standard reconstruction procedures were used, as discussed in the literature.[44−47] Since our present study was focused on isotopic analysis in single-phase reference materials, the dimensional accuracy of the spatial reconstruction was not critical. A voltage evolved tip radius was used, along with default reconstruction parameters, for each reconstruction. Corrected TOF spectra were generated in the IVAS Cal/Recon Wizard (CRW) and used for the isotopic analyses. Each TOF spectrum was filtered to remove as much of the multihit-detection-event-related ion signal as possible. The TOF spectra were then exported to *.csv files. A custom machine-learning-based adaptive peak fitting script was used to provide a mathematically defensible and repeatable method to fit the individual peaks comprising a family of peaks, i.e., the isotopic variants of a given ion species (e.g., $^{234}UO_2^{2+}$, $^{235}UO_2^{2+}$, $^{236}UO_2^{2+}$, $^{238}UO_2^{2+}$).[37] The script was designed to read the *.csv file, subset the spectrum to isolate a single family of peaks, fit each peak within the family, perform peak decompositions, and calculate the isotopic abundances. The script was written in the R programming language using RStudio.[48,49]

It is important to note that the instrument manufacturer uses different multihit detection event definitions for the corrected TOF spectrum (CRW) than for the *.ePOS ion data. It is our understanding, based on conversations with the manufacturer, that the detection event definitions in the CRW-corrected TOF spectrum are based solely on the timing signals. However, the *.ePOS data has additional filters applied to the data set and so redefines a fraction of the multihit events as single-hit events. The discrepancy in the number of single-hit detection events reported in each of the two versions of the ion data can be quite large. Isotopic analyses based on the CRW-corrected TOF spectrum are generally more accurate than analyses performed with the *.ePOS data.[37] Hence, we restrict our isotopic analyses to the CRW-corrected TOF spectrum exported from the IVAS. The application of our approach is thus currently limited to single-phase samples or easily parsed data sets, since the 3-D reconstructed data (*.ePOS data) cannot be used to perform the highest accuracy analyses.

Adaptive Peak Fitting. Due to the nature of an atom probe experiment, the peak forms encountered in the TOF spectrum (or mass spectrum) are governed by many factors, including materials properties, evaporation physics, and ion detection system response. Therefore, the peak form (including the tail and leading edge) can vary significantly between different ion species in the TOF spectrum (or mass spectrum).[37] This variation in peak form presents a challenge when performing accurate quantitative analyses, since it implies peak shape must be taken into account to obtain the most accurate analysis results, yet no single model peak form can be used to fit all peaks across the full range of the spectrum. Fortunately, the individual peaks comprising a family of peaks, i.e., isotopic variants of a given ion species, have nominally the same peak form. We can therefore assume that the spectrum in the region of a single family of peaks is a linear combination of the individual peaks comprising the family. An optimization algorithm can then be used to estimate the single peak form shared within the family of peaks. Our machine-learning-based adaptive peak fitting script employed the limited-memory Broyden−Fletcher−Goldfarb−Shanno algorithm with box constraints (L-BFGS-B[50]) to iteratively solve this optimization problem. Use of the L-BFGS-B algorithm significantly reduced both the run time and the number of fitting artifacts, relative to an earlier similar script that had employed a gradient descent optimization routine. For the interested reader, a detailed outline of the earlier script is provided in our prior work.[37] The peak positions were defined by the analyst, and the cost function to be minimized was the sum of squared residuals. A constant local background approximation was used under each family of peaks, as determined by averaging the ion counts in tens to hundreds of bins immediately to the left of the peak family. The box constraints were used to force all solutions to be non-negative and to ameliorate fitting artifacts. A bin width of 0.01 ns was used for each corrected TOF spectrum under analysis. Trials using a finer bin width did not significantly improve the analysis results. Each ion species was treated as a separate measurement for determining isotopic abundance. The results from multiple ion species in a given spectrum were then averaged together to produce the overall abundance measurement that was reported for that sample. It is important to emphasize the peak form is not assumed *a priori*, or defined by a mathematical formula, but rather is determined iteratively and channel-by-channel from the corrected TOF spectrum. Also, contributions from partially overlapping adjacent peaks can be separated from one another, even in the presence of complicated tail structures, without *a priori* knowledge of the

https://dx.doi.org/10.1021/acs.analchem.0c02273
Anal. Chem. 2020, 92, 11388−11395

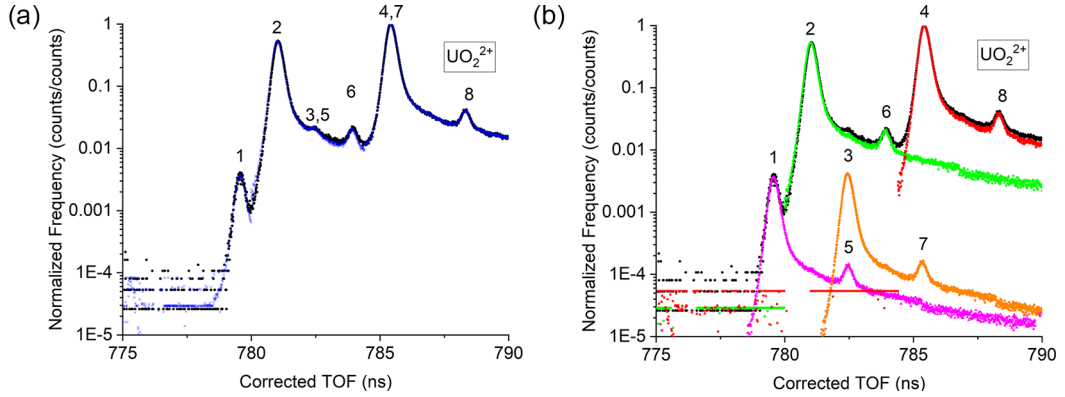

Figure 1. SRM U-350 corrected TOF spectrum in the region of the UO_2^{2+} ion species. (a) Black hexagons indicate the empirical data, and blue asterisks indicate the total result of the adaptive peak fitting algorithm. (b) The individual peaks determined by the adaptive peak fitting algorithm: red squares (A = 238), orange diamonds (A = 236), green circles (A = 235), and magenta triangles (A = 234). Peak indexing is as follows: (1) $^{234}UO_2^{2+}$, (2) $^{235}UO_2^{2+}$, (3) $^{236}UO_2^{2+}$, (4) $^{238}UO_2^{2+}$, (5) $^{234}UO_2H_2^{2+}$, (6) $^{235}UO_2H_2^{2+}$, (7) $^{236}UO_2H_2^{2+}$, (8) $^{238}UO_2H_2^{2+}$.

isotopic abundance—this is important for applications in which the isotopic abundance is the quantity to be measured.

RESULTS AND DISCUSSION

Single-Hit Corrected TOF Spectra. Replicate measurements were made for each reference material. Each replicate measurement was collected on a different individual particle: five particles for CRM 129-A, nine particles for SRM U-030A, seven particles for SRM U-350, and seven particles for SRM U-900 (Table S1). Only single-hit corrected TOF spectra (CRW) were used for isotopic analysis. For information purposes, one example mass spectrum is provided for each of the reference materials: Figure S1 (CRM 129-A), Figure S2 (SRM U-030A), Figure S3 (SRM U-350), and Figure S4 (SRM U-900). The uranium is only present as isotopic variants in uranium−oxygen and uranium−oxygen−hydrogen complex ion species. Other hydrogen and oxygen related ion species are also observed in the mass spectra. The predominant uranium ion species were UO^{2+}, UO_2^{2+}, UO_2^{+}, UO_3^{+}, and UO_4^{+}. We chose to use only the UO_2^{2+}, UO_2^{+}, and UO_3^{+} ion species for the isotopic analysis, since these were generally the peaks with the highest number of counts and so were present in all spectra.[13] The total uranium ion counts associated with each of these peak families are provided in Table S2. Table S3 provides the number of counts recorded for the maximum channel in each of the peaks used for isotopic analysis. The maximum channel ion counts are provided solely as additional information and should not be used for quantification, since using peak maxima alone for quantification tends to produce inaccurate results with poor repeatability. The sum of squared residuals values calculated by the peak fitting algorithm are provided in Table S4. The sum of squared residuals provides a measure of the amount of error between the fit and the empirical data—the sum of squared residuals will be zero for an exact fit. Overall, the quality of the fit achieved by the peak fitting script was excellent, as indicated by the accuracy of the isotopic analysis results and small residual values. Details specific to the spectra from each reference material will now be discussed.

Figure S5 shows the portion of the CRM 129-A (U-Nat) corrected TOF spectrum in the region of the UO_2^{2+} ion species. Four peaks are immediately identifiable in the spectrum: $^{234}UO_2^{2+}$, $^{235}UO_2^{2+}$, $^{238}UO_2^{2+}$, and $^{238}UO_2H_2^{2+}$. The peak fitting results are shown in Figure S6. The adaptive peak fitting algorithm was able to successfully discern the peak shape and decompose the overlapping peaks for each ion species. The hydride peaks, including the two buried hydride peaks $^{234}UO_2H_2^{2+}$ and $^{235}UO_2H_2^{2+}$, were successfully captured by the fit and properly associated with the respective parent isotope peaks during quantification. The ^{234}U, with an abundance of ∼0.0053%, is clearly visible in Figure S5. Similar peak fitting results are shown for the UO_2^{+} (Figure S7) and UO_3^{+} (Figure S8) ion species; however, the number of counts we generally recorded for these two ion species was not sufficient to capture the ^{234}U isotope in CRM 129-A. The ^{236}U isotopic abundance is too low to be detectable in the spectra recorded for CRM 129-A.

Figure S9 shows the portion of the SRM U-030A (LEU) corrected TOF spectrum in the region of the UO_2^{2+} ion species along with the peak fitting results. Five peaks are immediately identifiable in the spectrum: $^{234}UO_2^{2+}$, $^{235}UO_2^{2+}$, $^{238}UO_2^{2+}$, $^{235}UO_2H_2^{2+}$, and $^{238}UO_2H_2^{2+}$. As with the CRM 129-A spectra, the adaptive peak fitting algorithm was able to successfully discern the peak shape and decompose the overlapping peaks for each ion species. The hydride peaks, including the buried hydride peaks $^{234}UO_2H_2^{2+}$ and $^{235}UO_2H_2^{2+}$, were again successfully captured by the fit and properly associated with the respective parent isotope peaks during quantification. The ^{234}U isotope, with an abundance of ∼0.028%, is clearly visible in Figure S9. Similar peak fitting results are shown for the UO_2^{+} (Figure S10) and UO_3^{+} (Figure S11) ion species; however, for the example spectrum shown, the number of counts recorded for these two ion species was not sufficient to capture the ^{234}U isotope. The ^{236}U isotopic abundance is too low to be detectable in the spectra recorded for SRM U-030A.

Figure 1 shows the portion of the SRM U-350 (HEU) corrected TOF spectrum in the region of the UO_2^{2+} ion species along with the peak fitting results. Six peaks are immediately identifiable in the spectrum: $^{234}UO_2^{2+}$, $^{235}UO_2^{2+}$, $^{236}UO_2^{2+}$, $^{238}UO_2^{2+}$, $^{235}UO_2H_2^{2+}$, and $^{238}UO_2H_2^{2+}$. As with the other reference materials, the adaptive peak fitting algorithm was able to successfully discern the peak shape and decompose the overlapping peaks for each ion species.

All hydride peaks, including the two buried hydride peaks $^{234}UO_2H_2^{2+}$ and $^{236}UO_2H_2^{2+}$, were again successfully captured by the fit and properly associated with the respective parent isotope peaks during quantification. The ^{234}U isotope, with an

https://dx.doi.org/10.1021/acs.analchem.0c02273
Anal. Chem. 2020, 92, 11388−11395

Table 2. Comparison of Measured ^{235}U Abundance before and after Calibration

	abundance reference value (%)	precalibration measd rel error (%)	postcalibration measd rel error (%)	postcalibration min rel error (%)	postcalibration max rel error (%)
CRM 129-A	0.72087	−3.40	−0.11	−1.15	1.39
SRM U-030A	3.0404	−2.26	−0.11	−1.32	1.00
SRM U-350	35.19	0.02	0.18	0.00	0.38
SRM U-900	90.196	0.49	−0.13	−0.22	0.05

Table 3. Comparison of Measured ^{238}U Abundance before and after Calibration

	abundance reference value (%)	precalibration measd rel error (%)	postcalibration measd rel error (%)	postcalibration min rel error (%)	postcalibration max rel error (%)
SRM U-900	8.693	−1.45	−0.15	−1.10	0.78
SRM U-350	64.393	0.28	−0.05	−0.17	0.10
SRM U-030A	96.9312	0.09	−0.58	−0.62	−0.54
CRM 129-A	99.27382	0.03	−0.67	−0.68	−0.66

Table 4. Comparison of Measured ^{234}U Abundance before and after Calibration

	abundance reference value (%)	precalibration measd rel error (%)	postcalibration measd rel error (%)	postcalibration min rel error (%)	postcalibration max rel error (%)
CRM 129-A	0.0052962	NA	NA	NA	NA
SRM U-030A	0.02778	−19.38	−6.63	−10.60	−2.46
SRM U-350	0.2498	−2.01	1.54	−1.55	4.50
SRM U-900	0.7777	−2.49	−0.84	−2.01	0.19

abundance of ∼0.25%, is clearly visible in Figure 1. Similar peak fitting results are shown for the UO_2^+ (Figure S12) and UO_3^+ (Figure S13) ion species. The ^{236}U isotopic peak was also present in the spectra recorded for SRM U-350. As shown in Figure 1, the peak fitting script could capture the ^{236}U isotopic peak. However, for reasons discussed below, we generally did not attempt to quantify the ^{236}U abundance.

Figure S14 shows the portion of the SRM U-900 (HEU) corrected TOF spectrum in the region of the UO_2^{2+} ion species along with the peak fitting results. As with the SRM U-350 example, six peaks are immediately identifiable in the spectrum: $^{234}UO_2^{2+}$, $^{235}UO_2^{2+}$, $^{236}UO_2^{2+}$, $^{238}UO_2^{2+}$, $^{235}UO_2H_2^{2+}$, and $^{238}UO_2H_2^{2+}$. The adaptive peak fitting algorithm was, again, able to successfully discern the peak shape and decompose the overlapping peaks for each ion species. All hydride peaks, including the buried hydride peaks, e.g., $^{234}UO_2H_2^{2+}$, were again successfully captured by the fit and properly associated with the respective parent isotope peaks during quantification. The ^{234}U isotope, with an abundance of ∼0.78%, is clearly visible in Figure S14. Similar peak fitting results are shown for the UO_2^+ (Figure S15) and UO_3^+ (Figure S16) ion species. The ^{236}U isotopic variant peak was also present, as in the spectra recorded for SRM U-350. However, as will be discussed below, we generally omitted the ^{236}U isotope from the isotopic analyses.

Isotopic Analysis and Calibration Curves. The average measured isotopic abundance values can be plotted against the certified abundance values for both ^{235}U and ^{238}U for each reference material.[13] The resulting plot is shown in Figure S17, wherein the blue dashed line represents a linear fit to the data. The ^{235}U and ^{238}U measurements both track along the same linear trendline, indicating comparable measurement error can be expected for these two isotopes with our measurement procedure. Further, the slope of the trendline is near unity, indicating little bias on either the ^{235}U or the ^{238}U prior to the application of any calibration. However, as shown in Figure S18, there is a systematic bias on the ^{235}U abundance measurement. Here, we have plotted percent relative error as a function of isotopic abundance and indicated the range of measured values with error bars. Both the measurement bias and the range of measured values increase as the isotopic abundance decreases, as indicated by the blue dashed nonlinear curve fit line. The curve in Figure S18 was used as a calibration curve to further improve the accuracy of our measurements. Table 2 shows the pre- and postcalibration isotopic analysis results for ^{235}U. Across the full enrichment range explored (0.7−90% ^{235}U), the average measured percent relative error was less than ±0.2% after calibration. Further, no single ^{235}U measurement exceeded ±1.4% relative error after calibration.

If we plot the ^{238}U measurement results on Figure S18, the result is Figure S19. The ^{238}U appears to follow a similar trend to the ^{235}U measurements. Therefore, we can consider applying the same calibration curve to the ^{238}U measurements. The results are shown in Table 3. For all reference materials, the average measured percent relative error was less than ±0.7% after calibration. No single ^{238}U measurement exceeded ±1.1% relative error after calibration. However, the calibration increased the error on the two highest ^{238}U abundance values, indicating the calibration curve needs some further refinement. The overcorrected measurement values still had less than 0.7% relative error.

The ^{234}U was also measured. However, due to the low ^{234}U abundance (<1%), and related low number of ions, in each reference material, the ^{234}U peak was not always observed in the spectrum or in association with every uranium-containing ion species. Table S3 indicates for which data sets and peak families the ^{234}U peak was observed. The mathematical model used to define the ^{235}U and ^{238}U calibration curve could not be used for the ^{234}U abundance measurements. For each ^{235}U and ^{238}U measurement, measurements on three ion species were averaged to obtain a final measurement. With the ^{234}U measurements, this was not always possible. A separate calibration curve was generated for ^{234}U. The curve was

https://dx.doi.org/10.1021/acs.analchem.0c02273
Anal. Chem. 2020, 92, 11388−11395

compiled solely from abundance measurements made on the UO_2^{2+} ion species. Table 4 shows the ^{234}U analysis results. For SRM U-900, the ^{234}U abundance is 0.78%. As such, we might expect the accuracy to be similar to that for ^{235}U in CRM 129-A. Comparing the isotopic analysis results for these two materials shows that the accuracy of the ^{234}U (SRM U-900) results are consistent with the accuracy of the ^{235}U (CRM 129-A) results. Likewise, the ^{234}U abundance in SRM U-350 is of the same order of magnitude as the ^{234}U abundance in SRM U-900, and again, the accuracies of these two analyses are comparable. The accuracy reported for the ^{234}U abundance in SRM U-030A is significantly worse than that for SRM U-350 and SRM U-900—not surprising, since the ^{234}U abundance is an order of magnitude lower. Yet, we were still able to achieve an average accuracy of better than 7% relative error. While the ^{234}U peak was observed in one CRM 129-A spectrum, we chose not to report an analysis result, since the accuracy is expected to be worse than that observed for SRM U-030A and no replicate measurements were available to verify the result. Improving the accuracy of ^{234}U measurements and refining the ^{234}U calibration curve is a topic of continuing work.

The ^{236}U isotopic abundance is too low to be detected in the CRM 129-A and SRM U-030A spectra, but it is detectable in the HEU spectra. Generally, however, we chose to omit the ^{236}U isotope from analyses reported in this study. Omitting the ^{236}U isotope does not significantly affect the accuracy of the measurements made on other the isotopes, since the ^{236}U has an abundance of <0.33% in the HEU reference materials. However, exclusion of the ^{236}U isotope peak, from an analysis in which the isotope is clearly present, produces a small artifact peak on the tail of all other component peaks (e.g., Figures S14 and S15). This is due to the assumption in our peak fitting script that all isotopic variants of a given ion species have the same peak form, and the ^{236}U isotope was not specified as a peak to fit. The accurate quantification of the ^{236}U isotope in SRM U-350 and SRM U-900 presented several challenges that will continue to be part of our ongoing research effort. For example, Figure 1 and Figure S14 indicate that there is an isobaric overlap with a hydride peak, $^{234}UO_2H_2$. The problem is further compounded by the poor peak-to-background ratio for the ^{236}U isotope peak, since the peak sits on the trailing tail of the ^{235}U isotope peak. Also, Figures S13 and S16 indicate that there may also be an isobaric overlap with $^{235}UO_3H^+$, since evidence for this hydride is present on the tail of the $^{238}UO_3^+$ peak. Under our acquisition conditions, the UO_xH^{n+} ion species has only been observed in association with the UO_3^+ ion species. However, the abundance of the hydride ions may also change with the compound analyzed and the system vacuum conditions. As shown in Figure 1, the peak fitting script can be used to fit the ^{236}U peak. The results of these analysis attempts were correct within a factor of 2, but generally, the ^{236}U abundance was overestimated.

Figure S20 provides the theoretical estimated percent relative error $(1 - \sigma)$ as a function of the number of uranium atoms collected in an isotopic analysis of U_3O_8. We have assumed Poisson counting statistics and both 100% ionization and detection efficiency in this figure. The three reference lines each correspond to a different isotopic abundance value and have been chosen to match uranium at natural abundance: ^{238}U (black, lower), ^{235}U (red, middle), and ^{234}U (blue, upper). Therefore, for a given isotopic abundance, Figure S20 allows us to estimate the number of uranium atoms that would be required to produce an analysis result having a desired level of uncertainty. Likewise, for a given number of uranium atoms collected, and a specified isotopic abundance, Figure S20 allows us to estimate the uncertainty we would expect based solely on Poisson counting statistics. Using the uranium atom counts provided in Table S2, and weighted averages, we can estimate the average uncertainty that would be expected for each empirical abundance measurement, based solely on Poisson counting statistics. The results are provided in Table S5. Comparing the percent relative uncertainty measured for each isotope in each reference material (Tables 2−4) to the Poisson uncertainties reported in Table S5 shows that the postcalibration results are generally consistent with uncertainties approaching those limited primarily by the number of ion counts recorded. Our results are a significant improvement in accuracy over the ^{235}U and ^{234}U isotopic abundance measurements previously demonstrated for two of these U_3O_8 reference materials with an atom probe.[13] For example, we have demonstrated more than a 4-fold improvement in accuracy for minor isotopes (arbitrarily defined here as having an abundance of 0.1 > abundance > 0.007) prior to employing our calibration curve. Moreover, we have performed a more comprehensive study, using 7× as many samples, twice as many enrichment levels, and larger data sets to improve statistics and detection limits. Our method also offers several advantages over the full width at half-maximum based method proposed by Fahey et al.[13] For example, our use of single-hit data significantly reduces deadtime-related effects and multihit detection artifacts.[37] Also, our adaptive peak fitting algorithm permits full decomposition of partially overlapping peaks and proper attribution of hydride peaks to the parent isotopes for more accurate measurements.

Figure S20 can also be used to compare mass spectrometry techniques with different detection efficiencies. For example, suppose we wish to measure the isotopic abundance of ^{235}U in a sample of U-Nat (0.72%) with an uncertainty of ±0.7% relative error. Figure S20 indicates that ∼3.1×10^6 uranium atoms would be required to achieve the requisite level of uncertainty at 100% detection efficiency. For the APT analyses in this study, the detection efficiency was estimated to be ∼33%, after filtering the data sets to remove multihit detection events (∼50% prior to filtering). Thus, 3× as many ions need to be collected to achieve the same level of uncertainty (9.4×10^6 uranium atoms). A SIMS-like analysis, with a detection efficiency of 2%, would require 16.5× more ions (a volume ∼16.5× larger) to be collected than for APT (1.6×10^8 uranium atoms). While this is a hypothetical case, it demonstrates how APT can, in principle, deliver accurate isotopic analyses at a level of sensitivity and uncertainty that would require an analysis volume roughly an order of magnitude larger with another mass spectrometry technique.

CONCLUSIONS

We report a significant improvement in the isotopic analysis of uranium via atom probe mass spectrometry. To our knowledge, this is the first empirical atom probe study to demonstrate uranium isotopic analysis measurements, on uranium isotopic reference materials, with accuracy and repeatability approaching limits imposed predominantly by Poisson counting statistics, i.e., the number of uranium counts recorded. Further, we demonstrate this level of performance across a wide range of enrichment levels. Our measurement method has the potential to have a significant impact on

https://dx.doi.org/10.1021/acs.analchem.0c02273
Anal. Chem. 2020, 92, 11388−11395

isotopic analyses in the fields of isotope geochemistry, nuclear safety, and materials science.

The measurement method we proposed was tested for proof of concept against four elements in five natural materials in a prior manuscript. However, no replicate measurements were made as part of that study. Therefore, the present study sought to assess accuracy and repeatability (replicate measurements) with application to anthropogenic isotopic reference materials of uranium. These CRMs provide a uniform set of standards with a wide range of isotopic abundances and comprise one of the most extensive sets of isotopic standards with known absolute isotopic compositions for any element. The results indicate that APT can deliver accurate and repeatable uranium isotopic measurements for single sub-micrometer-scale U_3O_8 particles having ^{235}U abundance levels ranging from U-Nat (0.72% ^{235}U) to HEU (90% ^{235}U). Generally, the guidelines we proposed for APT isotopic analysis yielded ^{235}U and ^{238}U abundance values that are accurate to within 3.5% relative error. However, we observed a small systematic measurement bias as a function of isotopic abundance. The use of an empirically derived calibration curve can ameliorate this bias and push the limits of accuracy even further. The average accuracy we recorded after calibration for ^{235}U and ^{238}U was better than ±1% relative error, with no single measurement exceeding ±1.5% relative error. We have further shown that ^{234}U isotopic abundance can be accurately measured for an isotopic abundance as small as 0.25%. The ^{236}U isotope was detected in the HEU samples, for which it is present in an abundance >0.17%. Accurate quantification of ^{236}U isotope is part of an ongoing effort.

■ ASSOCIATED CONTENT

Supporting Information

The Supporting Information is available free of charge at https://pubs.acs.org/doi/10.1021/acs.analchem.0c02273.

> Specimen data acquisition conditions, example mass spectra for each reference material, example corrected time-of-flight spectra and peak fitting results for each reference material and ion species, tables of total uranium ion counts recorded for each specimen and ion species, and empirical calibration curves (PDF)

■ AUTHOR INFORMATION

Corresponding Author

Frederick Meisenkothen − *Materials Measurement Science Division, National Institute of Standards and Technology, Gaithersburg, Maryland 20899, United States;* orcid.org/0000-0003-4045-0949; Email: frederick.meisenkothen@nist.gov

Authors

Mark McLean − *Materials Measurement Science Division, National Institute of Standards and Technology, Gaithersburg, Maryland 20899, United States*

Irina Kalish − *Materials Measurement Science Division, National Institute of Standards and Technology, Gaithersburg, Maryland 20899, United States*

Daniel V. Samarov − *Statistical Engineering Division, National Institute of Standards and Technology, Gaithersburg, Maryland 20899, United States*

Eric B. Steel − *Materials Measurement Science Division, National Institute of Standards and Technology, Gaithersburg, Maryland 20899, United States*

Complete contact information is available at: https://pubs.acs.org/10.1021/acs.analchem.0c02273

Notes

Certain commercial equipment, instruments, or materials are identified in this paper in order to specify the experimental procedure adequately. Such identification is not intended to imply recommendation or endorsement by the National Institute of Standards and Technology, nor is it intended to imply that the materials or equipment identified are necessarily the best available for the purpose.

The authors declare no competing financial interest.

■ ACKNOWLEDGMENTS

The authors thank Adam Pintar of the National Institute of Standards and Technology Statistical Design, Analysis, and Modeling Group for helpful discussions regarding optimization problems and the R programming language. We are also grateful to Christopher Szakal and David Simons of the Material Measurement Laboratory for providing the isotopic reference materials used in this study. Helpful insights into multihit detection events definitions were provided by Ty Prosa and Rob Ulfig of CAMECA. This work was supported by the National Institute of Standards and Technology, Gaithersburg, MD, U.S.A.

■ REFERENCES

(1) Smith, G. D. W. Field Ion Microscopy and Atom Probe Microanalysis. In *ASM Handbook*, 9th ed.; Whan, R. E., Ed.; ASM International: Materials Park, OH, 1986; Vol. *10*, pp 583−602.

(2) Müller, E. W.; Panitz, J. A.; McLane, S. B. *Rev. Sci. Instrum.* **1968**, *39* (1), 83−86.

(3) Kelly, T. F.; Larson, D. J. *MRS Bull.* **2012**, *37* (2), 150−158.

(4) Kelly, T. F.; Larson, D. J. *Mater. Charact.* **2000**, *44* (1), 59−85.

(5) Zirakparvar, A. N.; Hexel, R. C.; Miskowiec, J. A.; Smith, B. J.; Ambrogio, W. M.; Duckworth, C. D.; Kapsimalis, R.; Ticknor, W. B. *Minerals* **2019**, *9* (5), 307.

(6) Kautz, E.; Burkes, D.; Joshi, V.; Lavender, C.; Devaraj, A. *Sci. Rep.* **2019**, *9* (1), 12302.

(7) Ronzani, A.-L.; Hubert, A.; Pointurier, F.; Marie, O.; Clavier, N.; Humbert, A.-C.; Aupiais, J.; Dacheux, N. *Rapid Commun. Mass Spectrom.* **2019**, *33* (5), 419−428.

(8) Valley, J. W.; Cavosie, A. J.; Ushikubo, T.; Reinhard, D. A.; Lawrence, D. F.; Larson, D. J.; Clifton, P. H.; Kelly, T. F.; Wilde, S. A.; Moser, D. E.; Spicuzza, M. J. *Nat. Geosci.* **2014**, *7* (3), 219−223.

(9) Valley, J. W.; Reinhard, D. A.; Cavosie, A. J.; Ushikubo, T.; Lawrence, D. F.; Larson, D. J.; Kelly, T. F.; Snoeyenbos, D. R.; Strickland, A. *Am. Mineral.* **2015**, *100*, 1355−1377.

(10) Saxey, D. W.; Moser, D. E.; Piazolo, S.; Reddy, S. M.; Valley, J. W. *Scr. Mater.* **2018**, *148*, 115−121.

(11) Bachhav, M.; Gan, J.; Keiser, D.; Giglio, J.; Jädernäs, D.; Leenaers, A.; Van den Berghe, S. *J. Nucl. Mater.* **2020**, *528*, 151853.

(12) Devaraj, A.; Kautz, E.; Kovarik, L.; Jana, S.; Lavender, C.; Joshi, V. APT and STEM Analysis of a Metallic Nuclear Fuel to Reveal the Influence of Grain Boundary Segregation on Kinetics of Discontinuous Precipitation. In *Proceedings of Atom Probe Tomography & Microscopy (APT&M) 2018, NIST Special Publication (SP) 2100-03*; Knipling, K. E., Meisenkothen, F., Steel, E. B., Eds.; National Institute of Standards and Technology: Gaithersburg, MD, 2018; p 195.

(13) Fahey, A. J.; Perea, D. E.; Bartrand, J.; Arey, B. W.; Thevuthasan, S. *J. Environ. Radioact.* **2016**, *153*, 206−213.

(14) Martin, T. L.; Martin, P.; Keatley, A.; Bagot, P. A. J.; Satou, Y.; Moody, M. P.; Scott, T. B. Atom Probe Tomography as a Nuclear Forensics Tool - Analysing Nanoparticulate Material from the Fukushima Region of Japan. In *Proceedings of Atom Probe Tomography & Microscopy (APT&M) 2018, NIST Special Publication (SP) 2100-03*; Knipling, K. E., Meisenkothen, F., Steel, E. B., Eds.; National Institute of Standards and Technology: Gaithersburg, MD, 2018; p 198.
(15) Valderrama, B.; Henderson, H. B.; Gan, J.; Manuel, M. V. *J. Nucl. Mater.* **2015**, *459*, 37−43.
(16) Bachhav, M.; Gan, J.; Miller, B.; Lingfeng, H.; Keiser, D. Understanding Behavior and Performance of Nuclear Fuels via Atom Probe Tomography. In *Proceedings of Atom Probe Tomography & Microscopy (APT&M) 2018, NIST Special Publication (SP) 2100-03*; Knipling, K. E., Meisenkothen, F., Steel, E. B., Eds.; National Institute of Standards and Technology: Gaithersburg, MD, 2018; p 197.
(17) Ironside, C. N.; Saxey, D. W.; Rickard, W. D. A.; Gray, C.; McGlynn, E.; Reddy, S. M.; Marks, N. A. *AIP Adv.* **2017**, *7* (2), 025004.
(18) Menand, A.; Kingham, D. R. *J. Phys. D: Appl. Phys.* **1984**, *17* (1), 203.
(19) Moutanabbir, O.; Isheim, D.; Seidman, D. N.; Kawamura, Y.; Itoh, K. M. *Appl. Phys. Lett.* **2011**, *98* (1), 013111.
(20) Shimizu, Y.; Kawamura, Y.; Uematsu, M.; Itoh, K. M.; Tomita, M.; Sasaki, M.; Uchida, H.; Takahashi, M. *J. Appl. Phys.* **2009**, *106* (7), 076102.
(21) Shimizu, Y.; Kawamura, Y.; Uematsu, M.; Tomita, M.; Kinno, T.; Okada, N.; Kato, M.; Uchida, H.; Takahashi, M.; Ito, H.; Ishikawa, H.; Ohji, Y.; Takamizawa, H.; Nagai, Y.; Itoh, K. M. *J. Appl. Phys.* **2011**, *109* (3), 036102.
(22) Lewis, J.; Isheim, D.; Floss, C.; Daulton, T.; Seidman, D. *Microsc. Microanal.* **2015**, *21* (S3), 39−40.
(23) Lewis, J. B.; Isheim, D.; Floss, C.; Seidman, D. N. *Ultramicroscopy* **2015**, *159*, 248−254.
(24) Lewis, J. B.; Isheim, D.; Floss, C.; Daulton, T.; Seidman, D. N.; Heck, P. R.; Davis, A. M.; Pellin, M. J.; Savina, M. R.; Hiller, J.; Mane, A.; Elam, J.; Auciello, O.; Stephan, T. Meteoritic Nanodiamond Analysis by Atom-Probe Tomography. Presented at the *43rd Lunar and Planetary Science Conference*, The Woodlands, Texas, March 19−23, 2012; LPI contribution no. 1659, i.d. 2192.
(25) Lewis, J. B.; Isheim, D.; Floss, C.; Daulton, T. L.; Seidman, D. N.; Heck, P. R.; Davis, A. M.; Pellin, M. J.; Savina, M. R.; Hiller, J.; et al. *Meteorit. Planet. Sci.* **2013**, 5296.
(26) Heck, P. R.; Pellen, M. J.; Davis, A. M.; Isheim, D.; Seidman, D. N.; Hiller, J.; Mane, A.; Elam, J.; Savina, M. R.; Auciello, O.; Stephan, T.; Larson, D. J.; Lewis, J.; Floss, C.; Daulton, T. L. Atom-Probe Tomographic Analysis: Towards Carbon Isotope Ratios in Individual Nanodiamonds. Presented at the *43rd Lunar and Planetary Science Conference*, The Woodlands, Texas, March 19−23, 2012; LPI contribution no. 1659, i.d. 1790.
(27) Diercks, D. R.; Gorman, B. P. *J. Phys. Chem. C* **2015**, *119* (35), 20623−20631.
(28) Diercks, D. R.; Gorman, B. P.; Kirchhofer, R.; Sanford, N.; Bertness, K.; Brubaker, M. *J. Appl. Phys.* **2013**, *114* (18), 184903.
(29) Exertier, F.; La Fontaine, A.; Corcoran, C.; Piazolo, S.; Belousova, E.; Peng, Z.; Gault, B.; Saxey, D. W.; Fougerouse, D.; Reddy, S. M.; Pedrazzini, S.; Bagot, P. A. J.; Moody, M. P.; Langelier, B.; Moser, D. E.; Botton, G. A.; Vogel, F.; Thompson, G. B.; Blanchard, P. T.; Chiaramonti, A. N.; Reinhard, D. A.; Rice, K. P.; Schreiber, D. K.; Kruska, K.; Wang, J.; Cairney, J. M. *Chem. Geol.* **2018**, *495*, 27−35.
(30) Kitaguchi, H. S.; Lozano-Perez, S.; Moody, M. P. *Ultramicroscopy* **2014**, *147*, 51−60.
(31) Laiginhas, F. A.; Perez-Huerta, A.; Martens, R. L.; Prosa, T. J.; Reinhard, D. *Microsc. Microanal.* **2015**, *21* (S3), 843−844.
(32) Lomboy, G. R.; Isheim, D.; Shah, S. P. Atom probe tomography for nanomodified Portland cement. In *Nanotechnology in Construction*; Sobolev, K., Shah, S. P., Eds.; Springer International Publishing: Cham, Switzerland, 2015; pp 79−85.
(33) Pérez-Huerta, A.; Laiginhas, F.; Reinhard, D. A.; Prosa, T. J.; Martens, R. L. *Micron* **2016**, *80*, 83−89.
(34) Riley, J. R.; Bernal, R. A.; Li, Q.; Espinosa, H. D.; Wang, G. T.; Lauhon, L. J. *ACS Nano* **2012**, *6* (5), 3898−3906.
(35) Devaraj, A.; Colby, R.; Hess, W. P.; Perea, D. E.; Thevuthasan, S. *J. Phys. Chem. Lett.* **2013**, *4* (6), 993−998.
(36) Hudson, D.; Smith, G. D. W.; Gault, B. *Ultramicroscopy* **2011**, *111* (6), 480−486.
(37) Meisenkothen, F.; Samarov, D. V.; Kalish, I.; Steel, E. B. *Ultramicroscopy* **2020**, *216*, 113018.
(38) Garner, E. I.; Machlan, L. A.; Shields, W. R. *Standard Reference Materials: Uranium Isotopic Standard Reference Materials (Certification of Uranium Isotopic Standard Reference Materials)*; National Bureau of Standards Special Publication 260-27; National Bureau of Standards: Washington, DC, 1971.
(39) Miller, M. K.; Russell, K. F.; Thompson, G. B. *Ultramicroscopy* **2005**, *102* (4), 287−298.
(40) Thompson, K.; Gorman, B.; Larson, D. J.; van Leer, B.; Hong, L. *Microsc. Microanal.* **2006**, *12* (S02), 1736−1737.
(41) Thompson, K.; Lawrence, D.; Larson, D. J.; Olson, J. D.; Kelly, T. F.; Gorman, B. *Ultramicroscopy* **2007**, *107* (2−3), 131−139.
(42) Cerezo, A.; Smith, G. D. W.; Clifton, P. H. *Appl. Phys. Lett.* **2006**, *88* (15), 154103.
(43) Larson, D. J.; Prosa, T. J.; Ulfig, R. M.; Geiser, B. P.; Kelly, T. F. *Local Electrode Atom Probe Tomography; A Users Guide*; Springer: New York, 2013; p 146.
(44) Bas, P.; Bostel, A.; Deconihout, B.; Blavette, D. *Appl. Surf. Sci.* **1995**, *87*−*88*, 298−304.
(45) Blavette, D.; Sarrau, J. M.; Bostel, A.; Gallot, J. *Rev. Phys. Appl.* **1982**, *17*, 435−440.
(46) Geiser, B. P.; Larson, D. J.; Oltman, E.; Gerstl, S.; Reinhard, D.; Kelly, T. F.; Prosa, T. J. *Microsc. Microanal.* **2009**, *15* (S2), 292−293.
(47) Larson, D. J.; Prosa, T. J.; Ulfig, R. M.; Geiser, B. P.; Kelly, T. F. *Local Electrode Atom Probe Tomography*; Springer: New York, 2013; pp 109−162.
(48) RStudio Team. *RStudio: Integrated Development for R*; RStudio, PBC: Boston, MA, 2020.
(49) R Core Team. *R: A Language and Environment for Statistical Computing*; R Foundation for Statistical Computing: Vienna, Austria, 2020.
(50) Byrd, R. H.; Lu, P.; Nocedal, J.; Zhu, C. *SIAM J. Sci. Comput.* **1995**, *16* (5), 1190−1208.

https://dx.doi.org/10.1021/acs.analchem.0c02273
Anal. Chem. 2020, 92, 11388−11395